Dalton Transactions

An international journal of inorganic chemistry

Accepted Manuscript

This article can be cited before page numbers have been issued, to do this please use: H. Hou, A. G. Rana, M. Minceva, M. Gil-Sepulcre, O. Ruediger, S. DeBeer, A. Garzon, M. Botifoll, Q. Ramasse, J. Arbiol, N. Romero, X. Sala, J. García-Antón, M. Tasbihi and F. Fresno, *Dalton Trans.*, 2026, DOI: 10.1039/D6DT00782A.

This is an Accepted Manuscript, which has been through the Royal Society of Chemistry peer review process and has been accepted for publication.

Accepted Manuscripts are published online shortly after acceptance, before technical editing, formatting and proof reading. Using this free service, authors can make their results available to the community, in citable form, before we publish the edited article. We will replace this Accepted Manuscript with the edited and formatted Advance Article as soon as it is available.

You can find more information about Accepted Manuscripts in the Information for Authors.

Please note that technical editing may introduce minor changes to the text and/or graphics, which may alter content. The journal's standard Terms & Conditions and the Ethical guidelines still apply. In no event shall the Royal Society of Chemistry be held responsible for any errors or omissions in this Accepted Manuscript or any consequences arising from the use of any information it contains.

ROYAL SOCIETY OF CHEMISTRY

rsc.li/dalton

Nickel and Platinum Modified Exfoliated Carbon Nitride as Photo-Thermal Catalysts for CO2 Hydrogenation

View Article Online
DOI: 10.1039/D6DT00782A

Heting Hou[1,2], Adeem Ghaffar Rana[3], Mirjana Minceva[3], Marcos Gil-Sepulcre[4], Olaf Rüdiger[5], Serena DeBeer[5], Alba Garzón Manjón[6], Marc Botifoll[6], Quentin Ramasse[8,9], Jordi Arbiol[6,7], Nuria Romero[2], Xavier Sala[2], Jordi García-Antón[2]*, Minoo Tasbihi[10]*, Fernando Fresno[11]*

[1] School of Chemical and Environmental Engineering, Liaoning University of Technology, Jinzhou, 121001 Liaoning Province, P. R. China
[2] Departament de Química, Unitat de Química Inorganica, Universitat Autonoma de Barcelona, 08193, Bellaterra, Barcelona, Spain
[3] Biotehrmodynamics, School of Sciences, Technical University of Munich, Maximus-von-Imhof-Forum 2, D-85354 Freising, Germany
[4] Departament de Química Orgànica, Facultat de Química, Universitat de València, Av. Vicent Andrés Estellés 19, 46100 Burjassot, Spain
[5] Max Planck Institute for Chemical Energy Conversion, Stiftstrasse 34-36, D-45470 Mülheim an der Ruhr, Germany.
[6] Catalan Institute of Nanoscience and Nanotechnology (ICN2) CSIC and BIST, Campus UAB, Bellaterra, 08193 Barcelona, Catalonia, Spain
[7] ICREA, Passeig de Lluís Companys 23, 08010 Barcelona, Catalonia, Spain
[8] SuperSTEM Laboratory, STFC Daresbury Campus, Daresbury, WA4 4AD, UK
[9] School of Chemical and Process Engineering & School of Physics and Astronomy, University of Leeds, Leeds, LS2 9JT, UK
[10] Department of Chemistry, Technical University Berlin, Straße des. 17 Juni, 10623 Berin, Germany. Present address: School of Technology and Architecture, SRH Berlin University of Applied Sciences, Sonnenallee 221, Berlin 12059, Germany
[11] Instituto de Catálisis y Petroleoquímica (ICP), CSIC, C/ Marie Curie 2, 28049 Madrid, Spain.
* Corresponding authors

View Article Online
DOI: 10.1039/D6DT00782A

Abstract

The photocatalytic conversion of carbon dioxide into value-added fuels and chemicals is a promising route to mitigate greenhouse gas emissions while enabling sustainable energy storage. This study investigates the use of catalysts composed of exfoliated graphitic carbon nitride modified with either single-atom Ni sites or Pt nanoparticles for photo-thermal CO_2 hydrogenation under combined light irradiation and thermal activation. The photocatalysts have been extensively characterized by different physico-chemical techniques, allowing the study of structure-activity relationships. Both metal-modified catalysts exhibit significantly enhanced CO_2 conversion compared to pristine g-C_3N_4, which is attributed to improved light absorption, reduced charge recombination, and the role of metals as catalytically active sites. However, the catalytic behaviour varies markedly depending on the metal. Pt nanoparticles promote a thermally driven pathway assisted by light, enhancing overall activity and favouring CO formation, whereas Ni single-atom sites preserve the photocatalytic character of the support and shift the selectivity of hydrogenation towards methanol rather than methane primarily obtained over metal-free C_3N_4. These findings indicate that the combined photonic and thermal energy inputs efficiently activate both CO_2 and H_2, accelerating reaction kinetics and modifying reaction pathways beyond those achieved in purely thermal or purely photocatalytic systems.

Keywords: Photothermal catalysis, CO_2 hydrogenation, Exfoliated Carbon Nitride, Platinum, Nickel

View Article Online
DOI: 10.1039/D6DT00782A

1. Introduction

The persistent rise in atmospheric carbon dioxide (CO_2) concentrations, driven by global industrialization and fossil fuel combustion, poses severe threats to climate stability and environmental health. Addressing this challenge demands innovative strategies that not only reduce CO_2 emissions but also transform this greenhouse gas into valuable fuels and chemicals, thereby establishing a sustainable carbon cycle.[1,2] Among these, catalytic CO_2 hydrogenation to value-added chemicals and fuels stands out as a promising approach.[3] However, conventional thermal catalytic processes often demand high temperatures and energy inputs, which limit their practical and environmental benefits. Recent advancements in photothermal catalysis have demonstrated the potential to overcome these limitations by synergistically combining light and thermal energy to drive CO_2 hydrogenation under milder conditions.[4,5] Photothermal catalysis leverages the localized heating and electronic excitation generated upon light absorption, which not only lowers reaction barriers but also enhances reaction rates and selectivity.[6,7] This dual-energy approach is especially effective for CO_2 activation. CO_2 is a notoriously challenging molecule due to its thermodynamic stability and kinetic inertness. This approach enables the production of a range of value-added products such as methane (CH_4), methanol (CH_3OH), and C_{2+} products.[6–8]

In this context, the design of efficient and robust photothermal catalysts is crucial.[9,10] A wide range of photocatalysts has been explored for this purpose, including transition and noble metal-based catalysts (e.g., Ni, Co, Fe, Cu, Pt, Rh, Pd) supported on various semiconductors or carbon-based materials.[5] For example, PtRh bimetallic nanoparticles on GaN nanowires/Si have demonstrated remarkable activity and selectivity for CO_2 hydrogenation to CO under concentrated light, leveraging the synergy between photogenerated carriers and photoinduced heat to reduce the apparent activation energy from 2.09 to 1.18 eV.[11] Similarly, nanostructured Pd@Nb_2O_5 catalysts have been shown to efficiently drive the reverse water-gas shift (RWGS) reaction under visible and near-infrared light, with H_2 dissociation on Pd and subsequent hydrogen spillover to Nb_2O_5 nanorods for CO_2 reduction.[12] Despite these advances, the role of the nature of metal sites is not yet fully understood in photothermal CO_2 hydrogenation. This distinction is critical, as the electronic structure, coordination environment, and metal-support interactions differ substantially between single-atom catalysts and nanoparticulate systems, potentially leading to different

View Article Online
DOI: 10.1039/D6DT00782A

activation mechanisms for CO_2 and H_2 as well as distinct product selectivities. In particular, elucidating how these different metal configurations influence the balance between photocatalytic and thermally driven pathways is essential for the development of more efficient and selective catalytic systems.[13]

Carbon-based supports have also been investigated due to their high surface area, chemical stability, and ability to disperse active metal sites. Exfoliated carbon nitride (exf-CN), a two-dimensional semiconductor with high chemical stability and visible light absorption, has emerged as an attractive support for catalytic metals.[14] Recently, graphitic carbon nitride-based materials decorated with transition metals such as platinum[15–19] or nickel[19–23] have been reported, and they have shown excellent catalytic performance for CO_2 reduction reactions, ethanol electrooxidation and the oxygen evolution reaction.[15-23] The incorporation of Ni and Pt onto exf-CN introduces abundant active sites for CO_2 adsorption and hydrogenation, while also improving charge separation and light utilization. Ni is valued for its low cost, earth abundance, and high catalytic activity, whereas Pt is recognized for its superior hydrogen activation and spillover effects, both of which are essential for efficient CO_2 hydrogenation.[5,24] Recent studies have shown that transition metals such as Ni and Pt play critical roles in CO_2 hydrogenation, each offering distinct advantages. Ni, when incorporated into oxide matrices such as In_2O_3, facilitates efficient H_2 dissociation and promotes methanol synthesis at relatively low temperatures, with high dispersion of Ni atoms suppressing undesired methane formation and enhancing product selectivity.[25] Pt, on the other hand, is renowned for its superior hydrogenation activity and ability to stabilize reaction intermediates, making it highly effective for producing higher hydrocarbons and oxygenates.[7] In this case, by modifying exf-CN with Ni or Pt, novel catalytic systems can be engineered to exploit both the photoactive nature of carbon nitride and the hydrogenation prowess of the metal nanoparticles. Such bifunctional catalysts are expected to exhibit enhanced activity and selectivity for CO_2 hydrogenation under photo-thermal conditions, leveraging the unique interfacial sites created at the metal-support boundary.[25]

This manuscript focuses on developing and characterizing hybrid catalysts composed of exfoliated carbon nitride modified with either Ni single atoms or Pt nanoparticles for photo-thermal CO_2 hydrogenation. By combining advanced characterization techniques with catalytic testing under controlled light and temperature conditions, the goal is to establish clear structure–activity–selectivity relationships and to identify the

View Article Online
DOI: 10.1039/D6DT00782A

specific roles of Ni and Pt in governing reaction pathways, with the long-term objective of identifying strategies for optimizing sustainable CO_2 conversion.

2. Experimental Section

2.1. Materials

Reagents handling and material synthesis were performed under inert conditions, either in a glove box (MBRAUN Unilab) under argon or using Schlenk-line and Fischer-Porter bottle techniques. Glassware was dried at 120 °C in an oven before use. The following chemicals were used as purchased: [Pt(dba)$_3$] (dba = dibenzylideneacetone) from Strem Chemicals, [Ni(cod)$_2$] (cod = cyclooctadiene) from Sigma-Aldrich, and hydrogen (H_2) gas from Abelló Linde (>99 999%). Melamine ($C_3H_6N_6$, 99%) was purchased from Alfa Aesar (Haverhill, MA, USA). Mesoporous graphitic carbon nitride (mpg-CN) was prepared as described in the next section. Tetrahydrofuran (THF) and hexane, purchased from Scharlab, were first dried and distilled and then degassed via freeze-pump-thaw cycles. Gases for catalytic experiments and chromatographic analyses were acquired from Air Liquide with N50 purity.

2.2. Catalyst synthesis

Synthesis of exfoliated graphitic carbon nitride (exf-g-CN). Bulk carbon nitride (g-CN) was synthesized by pre-thermal decomposition of melamine using the procedure established in a previous study.[14] Briefly, a closed crucible containing melamine was placed in a muffle furnace (Carbolite Gero, GPC 1200, Derbyshire, UK) for thermal decomposition. The heating programme consisted of two steps: heating up to 450 °C with a gradient of 2 °C min^{-1} and maintaining this temperature for 2 h. The sample was then heated to 550 °C at a rate of 2 °C min^{-1} and the temperature was maintained for 4 h. Bulk g-CN was crushed in a mortar and pestle, rinsed with ultrapure water, and dried at 80 °C overnight. Exf-g-CN was prepared from g-CN by a thermal treatment in which g-CN was placed in an open crucible in a muffle furnace for 2 h at 500 °C using a heating ramp of 2 °C min^{-1}.

Synthesis of Pt Nanoparticles and Ni Single Atom Catalysts supported on exf-g-CN

The preparation of Pt Nanoparticles (Pt NPs) and Ni Single Atom Catalysts (Ni SACs) supported on exfoliated carbon nitride was achieved through the utilization of the organometallic approach. For these experiments, 200 mg of exf-g-CN was weighed

View Article Online
DOI: 10.1039/D6DT00782A

and placed into a Fischer-Porter bottle that had been taken directly from the oven. After the sealing process, the reactor was connected to the vacuum line and then placed in the glove box. Then, 16 mL of THF were added to the Fischer-Porter, together with 0.012 mmol of $[Pt(dba)_3]$ (dba = dibenzylideneacetone) or 0.012 mmol of $[Ni(cod)_2]$ (cod = cyclooctadiene). Subsequently, the reactor was pressurized with 3 bar of H_2 at ambient temperature, and the reaction was allowed to run overnight. Once the H_2 pressure was released, a carbon-coated copper grid (400 mesh) was prepared for TEM analysis by the addition of a single drop of the colloidal solution. The exf-g-CN supported Pt or Ni hybrid materials were isolated and washed three times with hexane and then dried under vacuum to yield Pt@exf-g-CN and Ni@exf-g-CN, respectively.

2.3. Characterization

Nitrogen adsorption-desorption isotherms were recorded at 77 K in a Micromeritics ASAP2020 equipment after degassing the samples at 393 K.

The estimated weight percentages (wt%) of Pt on exf-g-CN were measured by using an ICP-OES equipment from Agilent (model Optima) at the Servei d'Anàlisi Química (SAQ) at the UAB.

High-resolution transmission electron microscopy (HRTEM) and high-angle annular dark-field (HAADF) images in scanning transmission electron microscopy (STEM) mode were acquired at the Electron Microscopy Unit of the Institut Català de Nanociència i Nanotecnologia (ICN2, Barcelona, Spain) using a FEI Tecnai G2 F20 microscope operated at 200 kV. TEM micrographs were processed with the Fiji-ImageJ image freeware. For each sample, a minimum of 200 NPs was measured. Additional HAADF imaging and electron energy-loss spectroscopy (EELS) were carried out at SuperSTEM using a Nion UltraSTEM 100 operated at 60 kV. The microscope optics were configured to form a 30 pA probe with a 30 mrad convergence half-angle, corresponding to an estimated probe size of 0.1 nm. The HAADF detector angular range was 90-185 mrad, while the EELS spectrometer, a Gatan Enfina retrofitted with a QuantumDetectors Merlin EELS hybrid-pixel detector, had a collection aperture with a 40 mrad semi-angle for acquiring the core-loss electron energy loss spectroscopy, used for compositional mapping and analysis of the Ni bonding environment. The native energy resolution of the cold-field emitter of the instrument is 0.3 eV.

EELS spectrum imaging was performed on selected regions of the C_3N_4 matrix. To improve the signal-to-noise ratio, the acquired spectrum images were denoised using

View Article Online
DOI: 10.1039/D6DT00782A

multivariate statistical analysis (MSA), retaining the first eight components for reconstruction. Spectra were extracted from individual pixels, the entire spectrum image, the material-containing region, and areas exhibiting the highest Ni signal intensity.

The extracted spectra were subsequently smoothed using a Savitzky-Golay filter (second-order polynomial, 9-pixel window). The continuum contribution beneath the Ni L_3 and L_2 edges was modelled using a Hartree-Slater cross-section and fitted individually to each spectrum using pre-edge, inter-edge, and post-edge fitting windows adapted to the spectral quality. Following background subtraction, the intensities of the Ni L_3 and L_2 edges were integrated within 10 eV windows centred on the corresponding peak maxima, and the resulting integrated intensities were used to calculate the L_3/L_2 ratio.

X-ray absorption spectroscopy at the Ni K-edge was used to analyze Ni@exf-g-CN before and after catalysis in fluorescence mode, and the reference samples and Ni foil, NiO, and $Ni(OH)_2$ references in transmission mode. Ni K-edge XAS spectra of Ni@exf-g-CN were collected in BL22 CLAESS at ALBA synchrotron (Spain), whereas the rest of the spectra were collected in the SAMBA beamline at Soleil synchrotron (France). All samples were prepared by dispersing the corresponding powder sample in cellulose in a pellet (φ = 6 mm). Afterwards, the samples were placed in the sample holder and sealed with 30 μm Kapton tape. Samples collected at BL22 CLAESS were measured using a Si (311) double crystal monochromator. The incident flux was *ca.* 5 x 10^{11} ph/sec. Incident energy was calibrated by assigning the inflection point of the corresponding metallic foil to 8333 eV. For the samples measured in the SAMBA beamline of the SOLEIL synchrotron, the incident energy was selected by a Si(200) double crystal monochromator. Incident flux was *ca.* 1 x 10^{10} ph/sec using a beam size of 1 mm × 0.5 mm. Fluorescence spectra were captured using a 36-element germanium detector. All the samples were measured at liquid N_2 temperature (77 K), and no evidence of radiation-induced damage on the samples was observed during the measurements. The incident energy was calibrated by assigning the inflection point of a Ni foil to 8333 eV. Final spectra were processed and normalized using Athena, and EXAFS fittings were carried out using Artemis, both included in the DEMETER package.[26]

View Article Online
DOI: 10.1039/D6DT00782A

2.4. Reaction tests

Photothermal CO_2 hydrogenation reactions were carried out at atmospheric pressure in an annular reactor composed of two concentric Pyrex glass tubes. The catalyst powders (ca. 50 mg) were coated onto the outer wall of the inner tube from ethanol suspensions. The reacting gas, composed of CO_2 and H_2 in a 1:4 ratio, flowed through the annular space over the catalyst layer with a rate of 40 mL min^{-1}. The reactor was placed in a lamp box equipped with four fluorescent white light tubes symmetrically surrounding it. A heating cartridge was placed inside the inner tube and connected to a temperature controller. The gas at the exit of the reactor was analyzed in line by means of a gas chromatograph (Agilent 8860) equipped with two columns (HP-MOLESIEVE and HP-PLOT-Q) and two detectors (TCD for CO_2, H_2 and CO, and FID for organic products) arranged in series, using helium as carrier gas. In a typical experiment, the gas feed was allowed to flow at room temperature in the dark until air was completely removed and CO_2 and H_2 concentrations stabilized. Then a temperature profile was initiated with ramps of 10 °C min^{-1} and plateaus at different values. At each plateau, dark and light steps were carried out. CO_2 conversion rates were calculated according to Eq. (1):

$$CO_2\ conversion\ rate = \sum(n_i \times r_i) \qquad \text{(Eq. 1)}$$

where n_i is the number of carbon atoms in the molecule of product *i* and r_i is the formation rate of product *i*.

3. Results and discussion

3.1. Synthesis of Pt NPs and Ni SACs supported on exf-CN

Pt NPs and Ni SACs on the surface of exfoliated graphitic carbon nitride were prepared by the so-called organometallic approach.[17] Briefly, either [Pt(dba)$_3$] (dba = dibenzylideneacetone) or [Ni(cod)$_2$] (cod= cyclooctadiene) were mixed with exf-CN in THF in a Fischer-Porter under 3 bar of H_2 and left overnight with vigorous stirring to give Pt@exf-g-CN and Ni@exf-g-CN.

3.2. Characterization of the photocatalysts

The metal content (wt% Pt or wt% Ni) present in Pt@exf-g-CN and Ni@exf-g-CN was quantified by ICP-OES, giving values of 1.2% and 0.34%, respectively (expected

View Article Online
DOI: 10.1039/D6DT00782A

values were 1.2% for Pt@exf-g-CN and 0.35% for Ni@exf-g-CN, which correspond to an equimolar metal loading). These values confirm the quantitative loading of Pt or Ni on exf-g-CN and thus a similar molar concentration of metal in the samples.

HRTEM was used to retrieve statistics on the particle size. Micrographs of Pt@exf-g-CN show small Pt NPs well dispersed on the surface of exf-g-CN (Figure 1), with an average Pt nanoparticle size of 1.5(0.5) nm. On the other hand, for Ni@exf-g-CN, no particles were observed on the surface of exf-g-CN, suggesting the presence of Ni SACs (Figure S1).

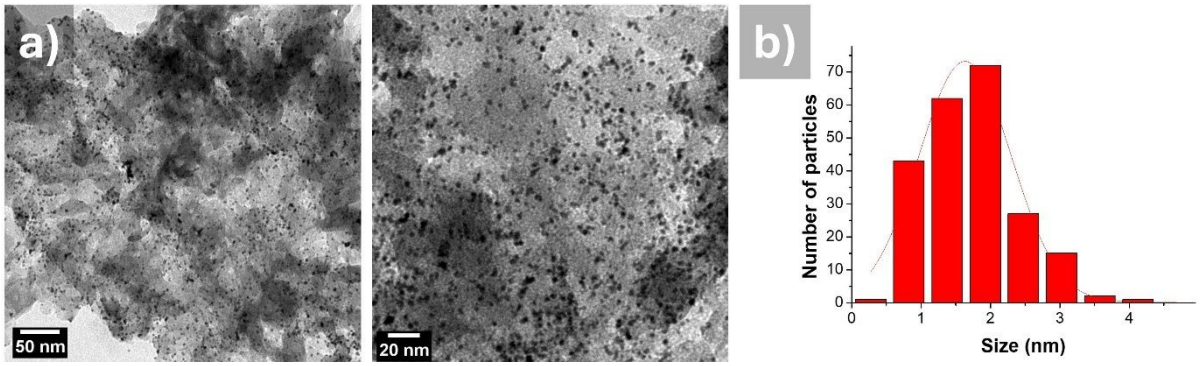

Figure 1. HR-TEM images (left) and size distribution (right) of Pt@exf-g-CN.

The Ni@exf-g-CN sample was further studied with high-angle annular dark-field scanning transmission electron microscopy (HAADF STEM) (Figure 2). Bright spots observed in HAADF STEM images indicate the presence of heavier atoms within the C_3N_4 matrix, contributing to a characteristic "galaxy-like" contrast. Electron energy loss spectroscopy (EELS) compositional analysis identifies these atoms as Ni (Figure 2). The spatial distribution of Ni within the C_3N_4 matrix is heterogeneous, with regions displaying varying concentrations. While some areas exhibit spectrally detectable Ni, others show levels below the detection threshold (~2 atoms/nm^3). Quantitatively, strong Ni signals were observed in approximately 20% of regions analysed, low but detectable levels in another 20%, and non-detectable Ni in the remaining 60%. In regions lacking the "galaxy-like" pattern, the absence of bright spots in the HAADF STEM images suggests Ni is either absent or below the detection limit.

EELS spectrum imaging was performed on several regions of the C_3N_4 matrix. In areas with a stronger Ni signal, both L_3 and L_2 edges were resolved, providing insights into the chemical nature of Ni. The key feature distinguishing NiO (Ni(II)) from metallic Ni

View Article Online
DOI: 10.1039/D6DT00782A

lies in the post-L_3 peak intensity, which falls to the background for NiO but not for metallic Ni, suggesting NiO as the dominant species (Figure 2d).

To further evaluate the EELS data, the Ni L_3/L_2 ratio was determined after appropriate spectral processing and background subtraction (see Experimental section for details). Despite the remaining noise, the ratio was found to oscillate around 3 in both the spatially averaged and single-pixel spectra, consistent with Ni(II) species.

However, the large error bars, arising from unavoidable noise and the very low signals intrinsic to single-atom systems, make it difficult to exclude the presence, at least in part, of metallic Ni(0). In addition, beam-induced damage to the C_3N_4 and its interaction with Ni may alter the observed valence state. Therefore, the EELS results should be interpreted with caution and complemented by XANES measurements.

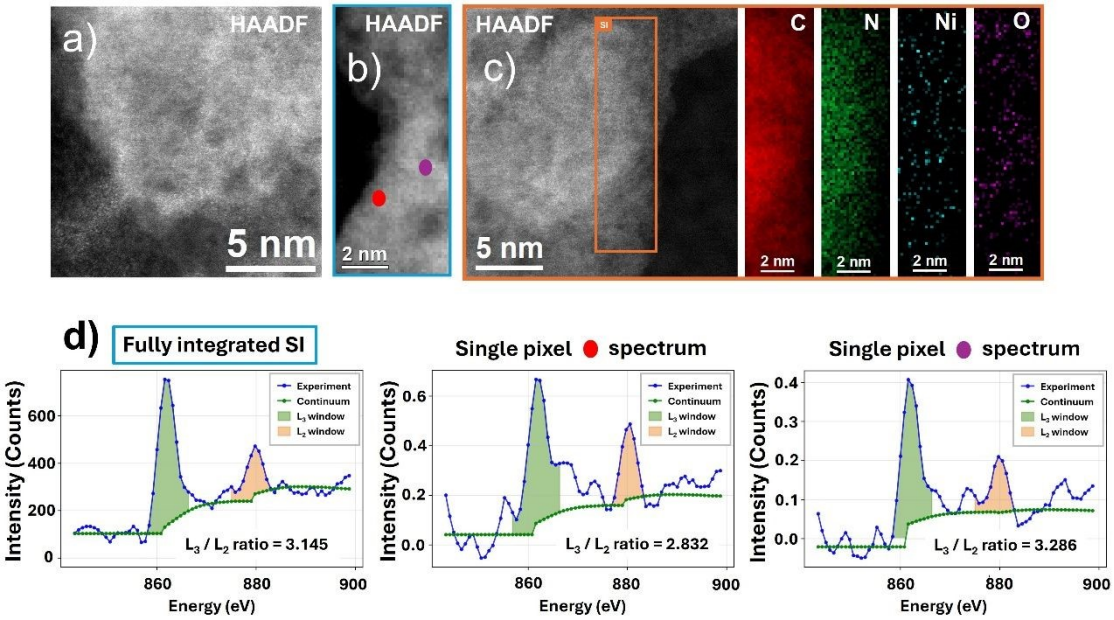

Figure 2. (a-c) HAADF-STEM micrographs displaying the heterogeneous Ni loading of the C_3N_4 matrix. a) General HAADF STEM view of the sample. b) HAADF STEM close view, where the bright spots highlight the presence of the Ni atomic distribution being heavier than the C and N atoms. c) HAADF STEM general view and corresponding EELS composition maps obtained on the orange rectangular area. The EELS composition maps reveal the dispersion of Ni atoms. d) EELS spectra obtained on whole and colour-indicated regions in b). Based on the near-background signal of L_2 we attribute the spectra to a majority of Ni(II) atoms, although the L_3/L_2 ratio also suggests the presence of metallic Ni atoms.

The electronic structure and local coordination environments of Ni@exf-g-CN were therefore further investigated using X-ray absorption spectroscopy (XAS), an ensemble-averaged technique sensitive to the oxidation state, geometry, and

View Article Online
DOI: 10.1039/D6DT00782A

coordination environment around the metal centers, complementing the local information provided by STEM-EELS, which confirmed local single-atom dispersions and the presence of Ni in regions where there are no NPs. The Ni K-edge X-ray absorption near-edge structure (XANES) spectrum of Ni@exf-g-CN shows an edge position close to that of Ni(II) references (Figure 3, left), indicative of an oxidation state close to (II), but showing remarkable differences in the 1s-to-3d pre-edge features and the white line profiles. Additionally, the steady increase of the signal after the 1s-to-3d pre-edge feature suggests the presence of traces of Ni(0) in the hybrid material, consistent with the error bars/scatter from the EELS analysis and becoming evident when compared to the sharp pre-edges observed in the pure NiO and $Ni(OH)_2$ references (Figure 3 left, inset).

A simple Ni(0) subtraction was carried out to roughly estimate the amount of metallic nickel present in our material by constructing a Ni@exf-g-CN spectrum, subtracting different amounts of Ni(0), and monitoring the pre-edge feature (see Figure S2). The analysis shows that the pre-edge feature of Ni@exf-g-CN spectrum started becoming negative after subtraction of a 6-7% of Ni(0), thus indicating the presence of approximately a 2-5% of Ni(0) in the Ni@exf-g-CN material. Extended X-ray absorption fine structure (EXAFS) spectroscopy was used to provide additional insights into the coordination environment of the metal centers (Figure 3, right).

The R-space spectrum of Ni@exf-g-CN is dominated by contributions from Ni-N/O scattering vectors at 2.1 Å, along with a significantly less intense peak at 2.5 Å, typically attributed to Ni-Ni distances in Ni(0) (see Table S1 and Figures S3 and S4). Interestingly, features at longer distances resulting from scattering with remote Ni centers (Ni-O-Ni) were not observed, strongly suggesting that the Ni centers are immobilized as isolated single atomic species.[27,28] Accordingly, the R-space spectrum was fitted using a simple model based on single atomic Ni(II) metal centers coordinated by four N-atoms, typically proposed for single atomic Ni systems in C_3N_4,[29] and consistent with the square planar geometry expected for Ni(II) d^8 metal centers, and containing 5% of Ni(0).

Finally, XAS analysis of Ni@exf-g-CN samples after the catalytic process (detailed below) was performed to evaluate the stability of the system (Figure 3). XANES spectrum (Figure 3, left) shows very similar features compared to the fresh Ni@exf-g-CN material, with only slight differences in terms of intensity, which can be attributed to self-absorption effects.[30] Importantly, FT-EXAFS spectrum (Figure 3, right) also

View Article Online
DOI: 10.1039/D6DT00782A

shows no additional scattering contributions after catalysis. The absence of longer scattering vectors at R > 2.5 Å and the presence of a stable ratio of Ni(II) and Ni(0) species before and after the catalytic process indicate that no significant aggregation of the active sites occurred during the reaction and that no detectable formation of Ni, NiO or $Ni(OH)_2$ particles took place, supporting the preservation of the local structure and composition of the active sites after catalysis.

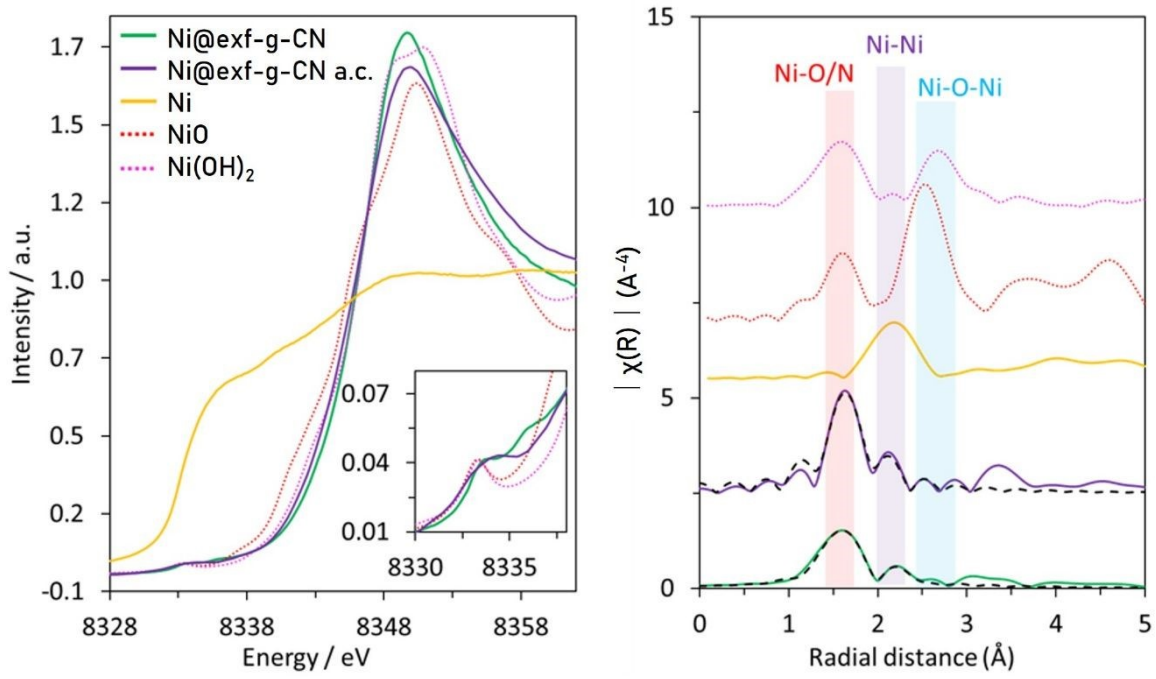

Figure 3. Left, Normalized Ni K-edge spectra of Ni@exf-g-CN (green), Ni@exf-g-CN after catalysis (purple), and Ni foil (yellow), NiO (red dotted line), and $Ni(OH)_2$ (pink dotted line) references. Inset: Zoom-in of the pre-edge region. Right, Fourier transforms of the k^2-weighted Ni EXAFS spectra (same colour code).

Regarding textural analysis, the three different samples exhibit the H3-type hysteresis loop, characteristic of non-rigid aggregations of plate-like particles,[31] as described before for exfoliated graphitic carbon nitride.[14] Only a slight reduction of BET surface area is observed upon metal particle deposition, with values of 147, 135, and 137 m^2g^{-1} for exf-g-CN and Pt- and Ni-modified samples, respectively.

3.3. Photo-thermal catalytic hydrogenation of CO_2

The reaction of CO_2 with H_2, in a continuous-flow annular reactor provided with internal heating and external visible light irradiation and in the presence of the different

View Article Online
DOI: 10.1039/D6DT00782A

catalysts, mainly led to the formation of CO, CH_4, CH_3OH, and dimethylether (DME), depending on the catalyst and the conditions, together with small amounts of C_2 products like ethane and ethylene. Figure 4 shows the obtained CO_2 conversion rates and product distributions over time at different temperatures and under dark or visible light irradiation over pure exf-g-CN, while the respective values obtained with the metal-loaded catalysts are represented in Figure 5.

It can be deduced from Figure 4 that exf-g-CN behaves exclusively as a photocatalyst, with activity ceasing upon irradiation cessation and decreasing with increasing temperature, a common feature in pure photocatalysis.[32] The obtained CO_2 conversion rate is considerably higher, though, than that obtained with a mesoporous graphitic carbon nitride photocatalyst using water instead of hydrogen as the electron donor.[17] Temperature modifies the main product of the reaction from methanol obtained at room temperature to methane at higher values, while irradiation has little effect on product distribution. Introduction of nickel (Figure 5) does not modify the intrinsic behaviour of the catalyst, in the sense that it still behaves as a photocatalyst with essentially no activity in dark conditions, regardless of the temperature, with the difference that methanol is favoured also at higher temperatures. Additionally, even if the overall activity is rather low, dimethyl ether appears as the main product at the maximum tested temperature of 350 ºC, contrary to the usual observation that nickel favours the Sabatier reaction in both thermal [33] and photothermal [34] conditions. This reveals a different reactivity of the Ni SACs compared to the pure exf-g-CN. The Ni-modified sample gives rise to a considerably higher reaction rate (nearly doubled) at room temperature, but this beneficial effect is lost when the temperature is increased.

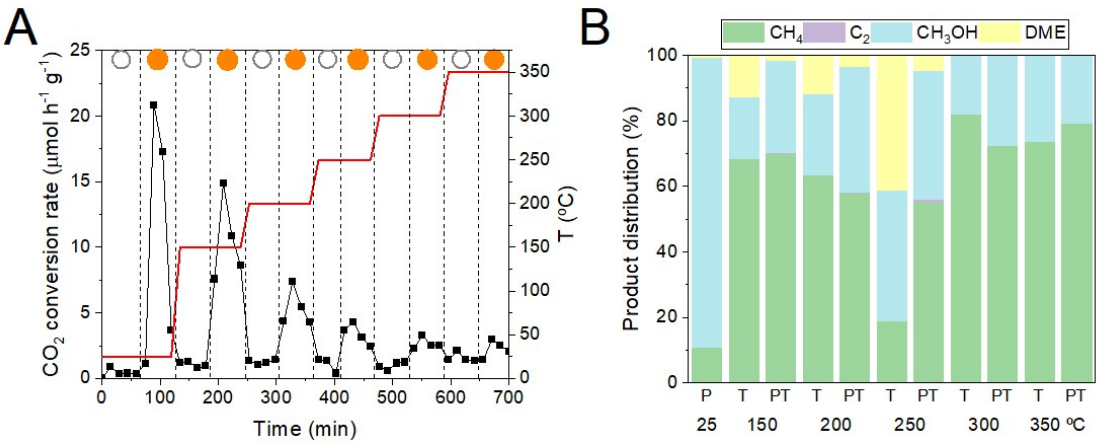

View Article Online
DOI: 10.1039/D6DT00782A

Figure 4. A: rate of CO_2 hydrogenation (symbols) at different temperatures (red lines) and under dark (void circles) or visible light irradiation (filled circles) over exf-g-CN. B: product distribution over exf-g-CN. “P”: photocatalytic; “T”: thermal; “PT”: photothermal.

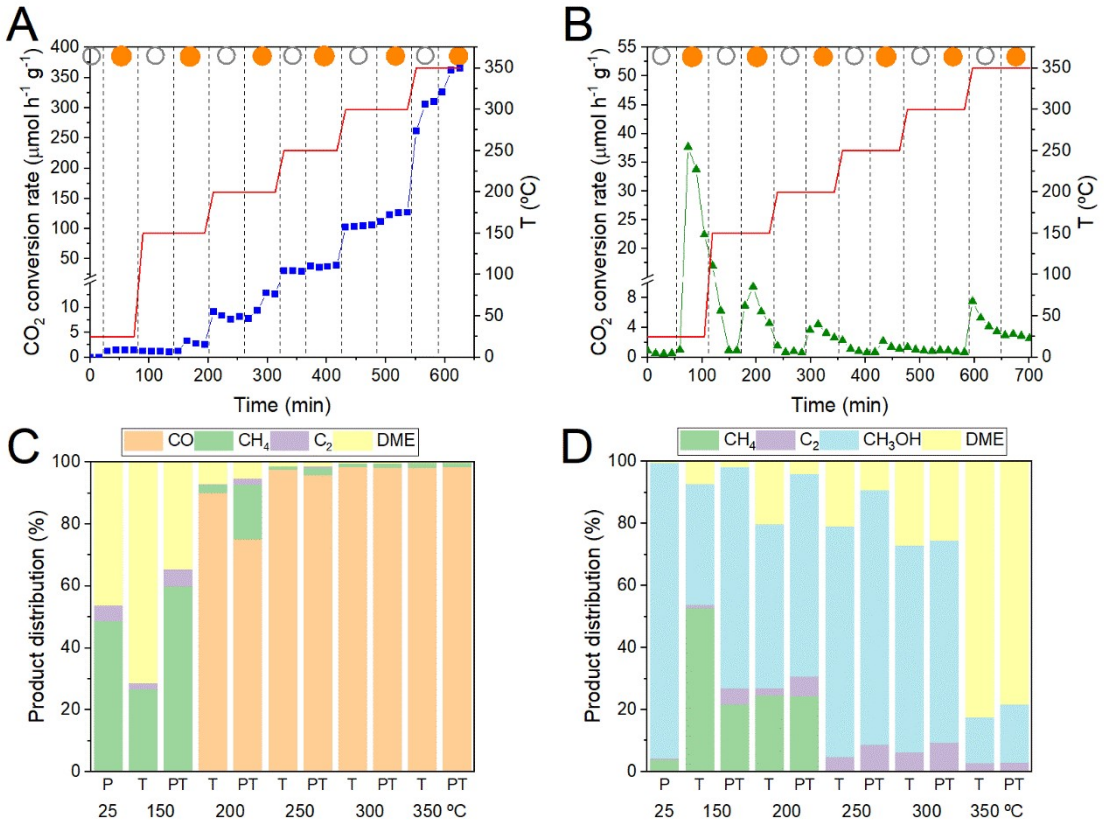

Figure 5. A, B: rate of CO_2 hydrogenation (symbols) at different temperatures (red lines) and under dark (void circles) or visible light irradiation (filled circles) over Pt@exf-g-CN and Ni@exf-g-CN catalysts, respectively. C, D: Product distribution over Pt@exf-g-CN and Ni@exf-g-CN catalysts, respectively. “P”: photocatalytic; “T”: thermal; “PT”: photothermal.

Contrary to the case of nickel, platinum-decorated exf-g-CN acts essentially as a thermal catalyst enhanced by visible light irradiation. At room temperature, low activity is observed, with selectivity shared nearly equally between methane and dimethyl ether. An effect of light over temperature is already noticeable at 150 ºC and is maintained at the rest of the assayed temperatures, with selectivity clearly biased towards CO from 200 ºC. A steady increase in activity is observed from this temperature, with reaction rates further increased by visible light irradiation at all tested temperatures.

Although spectroscopic insight into the reaction mechanism with the here-reported catalysts is still needed, differences in the promotion of the main products of CO_2 hydrogenation can be rationalized by the distinct reaction pathways that have been

View Article Online
DOI: 10.1039/D6DT00782A

previously proposed in the literature (Scheme S1).[35-37] The reaction is often proposed to begin with the hydrogenation of CO_2 to form a formate intermediate (HCOO*), a step identified as kinetically demanding under thermal conditions but facilitated under illumination, which has been reported to enhance charge transfer to adsorbed intermediates.[35] From this point, HCOO* may decompose to yield CO and H_2O through a reverse water-gas shift route, particularly when the availability of activated hydrogen and electrons is limited.[36] Alternatively, it may undergo further hydrogenation through oxygenated intermediates such as H_2COO*, H_2CO*, and CH_3O*, ultimately leading to methanol when C-O bonds are preserved along the pathway.[37] In contrast, deeper hydrogenation involving the transformation of CO* into HCO*, followed by successive reduction to CH_x species, leads to methane formation, with the CO* to HCO* step having been proposed to be promoted under electron-rich conditions generated by light irradiation.[35,36] Illumination may therefore play a dual role by enhancing charge carrier density and promoting charge transfer to adsorbed intermediates, which stabilizes reduced species such as $CO_2^{\delta-}$ and may facilitate hydrogenation steps with high electron demand. As a result, pathways toward methane are preferentially enhanced under conditions of high electron availability, whereas CO formation dominates when electron transfer is inefficient, and methanol selectivity is favoured when partially hydrogenated oxygenates are stabilized without complete C-O bond dissociation. The results observed with the present catalysts may therefore be related to a more efficient charge transfer between the photoactivated support and the metal species when Ni SACs are present, compared both with previously reported Ni catalysts,[34] and with the Pt nanoparticles synthesized in this work. This effect, combined with a temperature-dependent stabilization of partially hydrogenated oxygenates, could account for the observed product distributions. Dimethyl ether may result from further dehydration of methanol, which has also been reported to occur under photothermal conditions.[38]

4. Conclusions

In this study, Ni (single atoms) and Pt (nanoparticles) modified exfoliated graphitic carbon nitride (exf-g-CN) catalysts were synthesized using an organometallic approach and investigated for photo-thermal CO_2 hydrogenation under combined light irradiation and thermal activation. Pt@exf-g-CN exhibits small platinum nanoparticles on the surface of exf-g-CN. However, no particles were detected on the surface of exf-g-CN for Ni@exf-g-CN, suggesting the presence of Ni SACs, which was confirmed

View Article Online
DOI: 10.1039/D6DT00782A

through HAADF STEM and EELS and XAS analyses. The catalytic performance of exf-g-CN and its Ni- and Pt-modified counterparts for CO_2 hydrogenation was evaluated under varying temperatures and light conditions. The introduction of the metal components onto exf-g-CN significantly enhances CO_2 conversion by improving light absorption, facilitating charge separation, and providing active sites for H_2 activation. Pt nanoparticles primarily promote thermally driven pathways that are further enhanced under light irradiation, leading to increased activity and a shift in selectivity towards CO at elevated temperatures. In contrast, atomically dispersed Ni sites preserve the photocatalytic character of the material while modifying the reaction pathway, favouring methanol formation and suppressing the methane production observed for the bare support at moderate temperatures and predominantly producing dimethyl ether at higher ones. These findings indicate that the combined photonic and thermal energy inputs efficiently activate both CO_2 and H_2, accelerating reaction kinetics and modifying reaction pathways beyond those achieved in purely thermal or purely photocatalytic systems. Future work should focus on optimizing metal loading, as well as extending this approach to other metal-support combinations. In addition, deeper mechanistic studies under operando conditions will be essential to fully clarify the dynamic interactions between light, heat, and catalytic sites, and to advance the development of scalable photothermal systems for solar fuel production.

Acknowledgements

MGS, OR and SD thank the Max Planck Society for the funding. MGS acknowledges the support of the HORIZON-MSCA-2021-PF project TRUSol No. 101063820. MGS, OR and SD also acknowledge the CLAESS beamline at the ALBA Synchrotron (proposal No. 2021095409), SAMBA beamline at the SOLEIL (proposal No. 20221353), and beamline staff for support during the XAS measurements. ICN2 acknowledges funding from Generalitat de Catalunya 2021SGR00457. This study is part of the Advanced Materials programme and was supported by MCIN with funding from European Union NextGenerationEU (PRTR-C17.I1) and by Generalitat de Catalunya (In-CAEM Project). The authors thank support from the project AMaDE (PID2023-149158OB-C43), funded by MCIN/ AEI/10.13039/501100011033/. ICN2 is supported by the Severo Ochoa program from Spanish MCIN / AEI (Grant No.: CEX2021-001214-S) and is funded by the CERCA Program / Generalitat de Catalunya. AGM has received funding from Grant RYC2021-033479-I funded by

View Article Online
DOI: 10.1039/D6DT00782A

MCIN/AEI/ 10.13039/501100011033 and by European Union NextGenerationEU/PRTR. ICN2 is founding member of e-DREAM.[39] X. S. thanks ICREA for the ICREA Academia Prize 2020. X.S. and J.G.A. acknowledge funding from the Spanish Government (PID2023–146787OB-I00) and AGAUR (2023CLIMA-00011). FF thanks financial support from the Spanish State Agency for Research (AEI, 10.13039/501100011033) of the Ministry of Science, Innovation and Universities within the *RICHCO2* project (PID2023-152263OB-I00). SuperSTEM is the UK National Research Facility for Advanced Electron Microscopy, supported by the Engineering and Physical Sciences Research Council (EPSRC) under grant number EP/W021080/1.

References

1 Z. Zhang, X. Han, J. Zhang, Y. Dong, J. Zhao, Q. Xu and N. Zhang, *Nano Res.*, 2025, **18**, 94906998.
2 S. Roy, A. Cherevotan and S. C. Peter, *ACS Energy Lett.*, 2018, **3**, 1938–1966.
3 Y. Dong, R. Song, Z. Zhang, X. Han, B. Wang, S. Tao, J. Zhao, A. N. Alodhayb, Z. Chen, X. Yi and N. Zhang, *Cell Rep. Phys. Sci.*, 2024, **5**, 102227.
4 S. H. Choi, I. Song and W. J. Dong, *Energy Mater.*, **2025**, *5*, 500062.
5 Z. Xiao, P. Li, H. Zhang, S. Zhang, X. Tan, F. Ye, J. Gu, J. Zou and D. Wang, *Fuel*, 2024, **362**, 130906.
6 J. Zhai, Z. Xia, B. Zhou, H. Wu, T. Xue, X. Chen, J. Jiao, S. Jia, M. He and B. Han, *Nat. Commun.*, 2024, **15**, 1109.
7 Z. Zhang, X. Han, J. Zhang, Y. Dong, J. Zhao, Q. Xu and N. Zhang, *Nano Res.*, 2025, **18**, 94906998.
8 H.Kang, E.Brack, D.Gioffrè, A.Yakimov, C.Copéret, C.-J.Li, *ChemSusChem*, **2025**, 18, e202402646.
9 J. Z. Tai, H. Alias, A. Shamjuddin, M. S. M. Yusof and W. K. Fan, *J. Environ. Chem. Eng.*, 2025, **13**, 116291.
10 R. Guo, C. Xia, Z. Bi, Z. Zhang and W. Pan, *Fuel Process. Technol.*, 2023, **241**, 107617.
11 J. Li, B. Sheng, L. Qiu, J. Yang, P. Wang, Y. Li, T. Yu, H. Pan, Y. Li, M. Li, L. Zhu, X. Wang, Z. Huang and B. Zhou, *Chem. Sci.*, 2024, **15**, 7714–7724.
12 J. Jia, P. G. O'Brien, L. He, Q. Qiao, T. Fei, L. M. Reyes, T. E. Burrow, Y. Dong, K. Liao, M. Varela, S. J. Pennycook, M. Hmadeh, A. S. Helmy, N. P. Kherani, D. D. Perovic and G. A. Ozin, *Adv. Sci.*, **2016**, 3: 1600189.
13 H. He, Y. Ren, R. Peng, H. Zhang, Y. Zhu, X. Liu, J. Zhou, L. Duan, Y. Si, M. Liu, D. Jing and N. Li, *Adv. Mater.*, 2026, **38**, e23060.
14 A. G. Rana, M. Tasbihi, M. Schwarze and M. Minceva, *Catalysts*, 2021, **11**, 662.
15 M. Brugia, A. Gasparotto, M. Benedet, D. Barreca, G. A. Rizzi and C. Maccato, *Surf. Sci. Spectra*, 2024, **31**, 024002.
16 L. Cheng, P. Zhang, Q. Wen, J. Fan and Q. Xiang, *Chin. J. Catal.*, 2022, **43**, 451–460.
17 M. Tasbihi, F. Fresno, I. Álvarez-Prada, A. Acharjya, A. Thomas, L. Escriche, N. Romero, X. Sala, V. A. De La Peña O'Shea and J. García-Antón, *J. CO2 Util.*, 2021, **50**, 101574.
18 X. Shi, Y. Huang, Y. Bo, D. Duan, Z. Wang, J. Cao, G. Zhu, W. Ho, L. Wang, T. Huang and Y. Xiong, *Angew. Chem. Int. Ed.*, 2022, **61**, e202203063.
19 M. Brugia, M. Benedet, G. A. Rizzi, A. Gasparotto, D. Barreca, O. I. Lebedev and C. Maccato, *ChemSusChem*, 2024, **17**, e202401041.
20 E. Scattolin, M. Benedet, D. Barreca, G. A. Rizzi, A. Gasparotto and C. Maccato, *Surf. Sci. Spectra*, 2024, **31**, 024001.
21 C. Guo, T. Zhang, X. Deng, X. Liang, W. Guo, X. Lu and C. L. Wu, *ChemSusChem*, 2019, **12**, 5126–5132.

22 E. Scattolin, M. Benedet, G. A. Rizzi, A. Gasparotto, O. I. Lebedev, D. Barreca and C. Maccato, *ChemSusChem*, 2024, **17**, e202400948.
23 Z. Refaat, M. E. Saied, A. O. A. E. Naga, S. A. Shaban, H. B. Hassan, M. R. Shehata and F. Y. E. Kady, *Sci. Rep.*, 2023, **13**, 4855.
24 H. Wang, S. Fu, B. Shang, S. Jeon, Y. Zhong, N. J. Harmon, C. Choi, E. A. Stach, H. Wang, *Angew. Chem. Int. Ed.*2023, 62, e202305251.
25 M. Ren, Y. Zhang, X. Wang and H. Qiu, *Catalysts*, 2022, **12**, 403.
26 B. Ravel and M. Newville, *J. Synchrotron Radiat.*, 2005, **12**, 537–541.
27 K. Khan, X. Yan, Q. Yu, S.-H. Bae, J. J. White, J. Liu, T. Liu, C. Sun, J. Kim, H.-M. Cheng, Y. Wang, B. Liu, K. Amine, X. Pan and Z. Luo, *Nano Energy*, 2021, **90**, 106488.
28 X. Zhang, H. Su, P. Cui, Y. Cao, Z. Teng, Q. Zhang, Y. Wang, Y. Feng, R. Feng, J. Hou, X. Zhou, P. Ma, H. Hu, K. Wang, C. Wang, L. Gan, Y. Zhao, Q. Liu, T. Zhang and K. Zheng, *Nat. Commun.*, 2023, **14**, 7115.
29 H.-Y. Jeong, M. Balamurugan, V. S. K. Choutipalli, E. Jeong, V. Subramanian, U. Sim and K. T. Nam, *J. Mater. Chem. A*, 2019, **7**, 10651–10661.
30 M. Pompa, A.-M. Flank, R. Delaunay, A. Bianconi and P. Lagarde, *Phys. B Condens. Matter*, 1995, **208–209**, 143–144.
31 M. Thommes, K. Kaneko, A. V Neimark, J. P. Olivier, F. Rodriguez-reinoso, J. Rouquerol and K. S. W. Sing, *Pure Appl. Chem.*, 2015, **87**, 1051–1069.
32 J.-M. Herrmann, *Appl. Catal. B Environ.*, 2010, **99**, 461–468.
33 A. Quindimil, U. De-La-Torre, B. Pereda-Ayo, A. Davó-Quiñonero, E. Bailón-García, D. Lozano-Castelló, J. A. González-Marcos, A. Bueno-López and J. R. González-Velasco, *Catal. Today*, 2020, **356**, 419–432.
34 E. Alfonso-González, A. Iglesias-Juez, F. Fresno and J. M. Coronado, *ChemCatChem*, **2024**, 16, e202401218.
35 Y. Li, Z. Rao, Z. Liu, J. Zeng, W. Bao, Z. Wang, J. Li, F. Yu, B. Dai and Y. Zhou, *ChemCatChem*, 2022, **14**, e202200182.
36 Q. Li, C. Wang, H. Wang, J. Chen, J. Chen and H. Jia, *Angew. Chem. Int. Ed.*, 2024, **63**, e202318166.
37 B. Xie, R. J. Wong, T. H. Tan, M. Higham, E. K. Gibson, D. Decarolis, J. Callison, K.-F. Aguey-Zinsou, M. Bowker, C. R. A. Catlow, J. Scott and R. Amal, *Nat. Commun.*, 2020, **11**, 1615.
38 X. Zhang, D. Luo, Y. Liu, X. Wang, H. Hu, J. Ye and D. Wang, *J. Photochem. Photobiol. Chem.*, 2023, **441**, 114728.
39 R. Ciancio, R. E. Dunin-Borkowski, E. Snoeck, M. Kociak, R. Holmestad, J. Verbeeck, A. I. Kirkland, G. Kothleitner and J. Arbiol, *Microsc. Microanal.*, 2022, **28**, 2900–2902.

View Article Online
DOI: 10.1039/D6DT00782A

Data availability

Data supporting this study are included in the article and its Electronic Supplementary Information (ESI). No references are cited in the ESI.